

SURFACE-ELECTRODE ARCHITECTURE FOR ION-TRAP QUANTUM INFORMATION PROCESSING

J. CHIAVERINI,^a R. B. BLAKESTAD, J. BRITTON, J. D. JOST, C. LANGER,
D. LEIBFRIED, R. OZERI, and D. J. WINELAND
NIST, Time and Frequency Division, Ion Storage Group
325 Broadway, Boulder, CO 80305 USA

Received January 26, 2005

Revised June 7, 2005

We investigate a surface-mounted electrode geometry for miniature linear radio frequency Paul ion traps. The electrodes reside in a single plane on a substrate, and the pseudopotential minimum of the trap is located above the substrate at a distance on the order of the electrodes' lateral extent or separation. This architecture provides the possibility to apply standard microfabrication principles to the construction of multiplexed ion traps, which may be of particular importance in light of recent proposals for large-scale quantum computation based on individual trapped ions.

Keywords: ion traps, quantum computation, quantum information, microfabrication, trapped ions

Communicated by: I. Cirac & R. Blatt

1 Introduction

One promising architecture for quantum information processing (QIP) is the trapping and manipulation of individual atomic ions in radio frequency (RF) linear Paul traps [1, 2, 3, 4, 5, 6, 7]. To become a viable implementation for the execution of large-scale quantum algorithms, this scheme requires the precise control of many ions as quantum bits (qubits). In one possible implementation [2, 3], ion qubits are held in separate trapping regions and moved around at will, so that selected ions may be brought into mutual proximity for the application of quantum gates and separated again.

The proposed method [2, 3] involves holding ion qubits in “memory” zones of a trap array (see Fig. 1). Ions to be used in a particular gate operation would be moved from the memory zones to “processor” zones. Quantum gates could be performed on a few ions in such a processor zone by means of entanglement of the motional modes of these ions with their internal qubit states as, for example, in [1, 6, 8]. Single bit operations can be performed on ions that have been moved separately into such a trapping region. For both single- and multi-qubit operations, individual addressing of the ions through tight laser-beam focussing would not be required [3]. With such a design, highly parallel processing is possible (there can be many zones with interchangeable roles), and separate (shielded) regions of the

^aemail: john.chiaverini@boulder.nist.gov

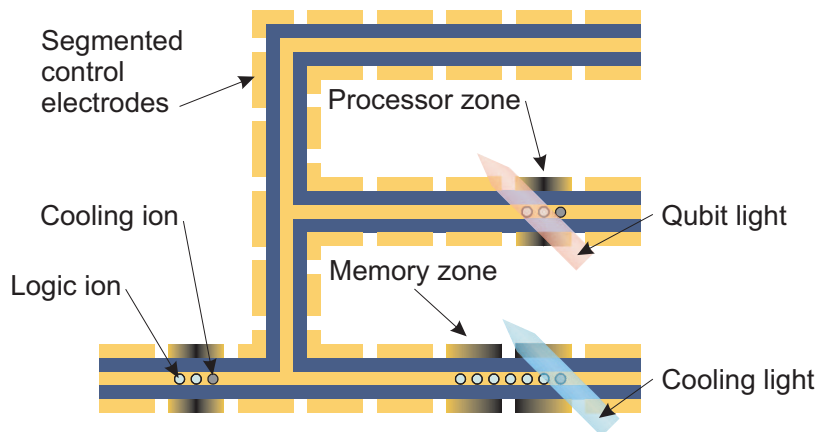


Fig. 1. Schematic diagram of proposed large-scale ion trap array for quantum information processing [2, 3]. Segmented control electrodes allow logic ions (lighter-colored circles) to be transferred to and from “memory” and “processor” regions. After transport, ions are sympathetically re-cooled by means of cooling ions (darker-colored circles). The laser light used for qubit operations has a frequency different from that used for sympathetic cooling to minimize decoherence of the qubit ions by the cooling light. The basic electrode layout depicted here is a “five-wire” surface geometry (described below in Sec. 4); dark-colored electrodes are radio-frequency (RF) electrodes, and light-colored control electrodes are held at RF ground.

array may be used for readout of ancilla qubits during a computation so that the effect of scattered light from this process on memory ions will be minimized. It appears that rapid ion transportation through, and ion separation in, such an array leads to heating of the motional modes [9]; therefore the ions will have to be sympathetically cooled by “refrigerator” ions after transport [2, 3, 10, 11, 12] and before additional entangling operations. These requirements imply a physical architecture in which there are many distinct but interconnected trapping regions. The separation, transportation, and recombination of ions must be controlled by means of time-varying potentials on control electrodes linking these trapping regions.

Current linear ion trap designs [9, 13, 14, 15, 16, 17, 18, 19] are somewhat bulky, require considerable time and effort for construction, and are not easily extendable to more complicated layouts. Here we describe an alternative approach, one that employs methods of microfabrication to construct traps of planar geometry that are scalable (in both electrode size and trap-array extent) and somewhat simpler in design. In Sec. 2 we describe the properties of a typically-used four-rod trap geometry. In Sec. 3, layered-electrode geometries are discussed, and in Sec. 4 we posit a surface-mounted electrode architecture to address some of the inherent problems in the other structures. Section 5 contains a discussion of trapping parameters for the surface electrode design, and in Sec. 6 we describe a possible implementation using microfabrication techniques. We propose a simple benefit of this design for studies of ion heating due to electrode surface quality in Sec. 7.

2 Background

A typical design for a linear RF Paul trap [20] consists of four parallel linear electrodes, each equidistant from the trap axis and from its two nearest neighbors. Two of these electrodes

(in opposite positions about the trap axis) are driven by an RF potential, and the other two “control” electrodes are maintained at RF ground (see Fig. 2). This geometry creates the required quadrupolar RF field for ponderomotive confinement in the lateral directions. The two control electrodes are segmented along their length, and static potentials can be applied to these segments to provide longitudinal confinement.

The classical motion of a charged particle in such a trap can be determined by solving the Mathieu equations associated with the equations of motion of the particle in the applied potential [21, 22]. The parameters of the ion traps typically employed allow a more intuitive solution. This is the pseudopotential approximation [23, 24], in which ions are bound through a ponderomotive potential

$$U_{2D}(\mathbf{r}) = \frac{Q^2}{2m\Omega^2} \langle E^2(\mathbf{r}) \rangle \quad (1)$$

at position \mathbf{r} , where Q is the particle’s charge, m is its mass, Ω is the RF drive frequency (rad/s), and E is the magnitude of the applied electric field. For the standard quadrupole geometry close to the trap center, this becomes

$$U_{2D}(\mathbf{r}) = \frac{Q^2 V_0^2}{4m\Omega^2 R^4} (x^2 + y^2) \quad (2)$$

if $\mathbf{r} \equiv x\hat{\mathbf{x}} + y\hat{\mathbf{y}}$ is the displacement from the trap axis. Here V_0 is the peak amplitude of the RF potential and R is approximately equal to the distance from the center of the trap to the nearest electrode surface. This pseudopotential confines ions in two dimensions, and its curvature (second spatial derivative) at the trapping location dictates their oscillation frequency.

For typical trap parameters, one obtains the following for the motion along either of the two radial directions ($i = \{1, 2\}$), up to a relative phase:

$$x_i(t) \approx X_{i0} \cos \omega_i t \left[1 + \frac{q_i}{2} \sin \Omega t \right]. \quad (3)$$

In this equation the x_i are the usual coordinates x and y , the X_{i0} are the pseudopotential oscillation amplitudes in each direction, and the ω_i are the pseudopotential oscillation frequencies (less than half the RF drive frequency). The parameter q_i is a normalized trap strength

$$q_1 = -q_2 = \frac{2QV_0}{m\Omega^2 R^2}, \quad (4)$$

with a typical magnitude small compared to 1. Hence the motion in the radial directions is composed of motion $X_{i0} \cos \omega_i t$ at frequency ω_i , dubbed the “secular” motion, with excursions of smaller amplitude at the RF frequency. This superimposed motion is referred to as “micromotion,” and its amplitude is proportional to the ion’s radial secular motion displacement from the trap center. The pseudopotential picture effectively ignores ion micromotion, which is added as a perturbation in Eq. 3.

Figure 2 displays equal-pseudopotential contours for a linear RF Paul trap of standard, four-rod geometry. The potential at the trapping region in the center is approximately quadratic with a constant curvature, independent of direction in the x - y plane. Potential local maxima (saddle points) exist at large displacements from the center at four locations

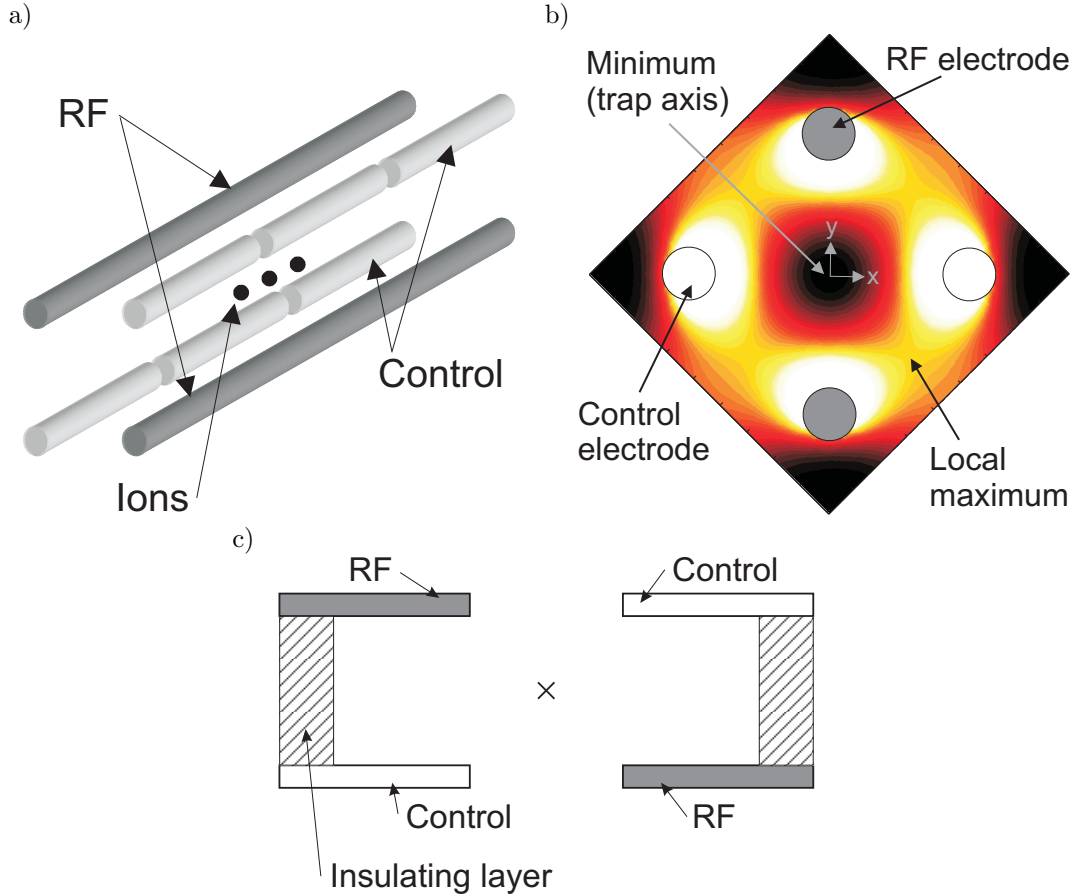


Fig. 2. Standard four-rod, linear RF quadrupole trap. (a) Perspective drawing of the geometry of this type of trap. (b) Radial pseudopotential contours (looking down the axis) of the four-rod trap. Colors from black to white indicate low to high pseudopotential, respectively. For clarity, contours are not shown for pseudopotential values above an arbitrary maximum. (c) One implementation of the four-rod design using two conducting layers separated by an insulating layer [9].

between the trap electrodes and may provide escape pathways for energetic ions. Ions can be readily trapped and cooled in current traps if these barriers ensure a trap depth of ~ 1 eV or larger.

Current and past implementations of this four-rod design have involved, for example, macroscopic rods in a quadrupole formation [25, 26] and a quadrupole formed by the inside edges of slots cut into pairs of alumina wafers [9] as well as other designs [13, 14, 16, 17, 18, 19]. All of these devices involve macroscopic machining of some sort. Such traps function well, but they do not appear to offer a path toward the smaller, more complicated devices that will be necessary for large-scale QIP with trapped ions.

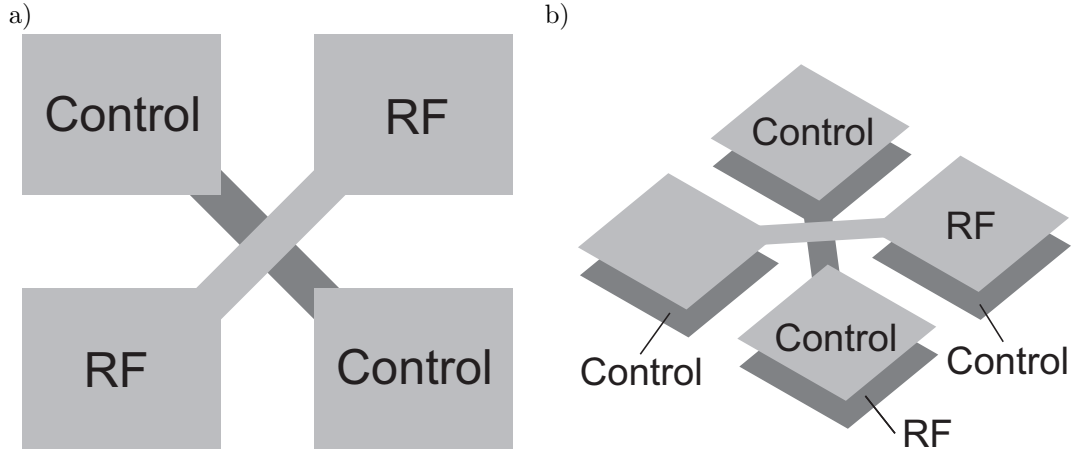


Fig. 3. Schematic diagram of modified two-layer cross to maintain a trapping potential at the center of the cross. Away from the cross, each of the four linear trapping regions consists of a four-rod linear trap implemented with two conducting layers as in Fig. 2c. The ions would be trapped halfway between the two layers. (a) Top view showing diagonal bridges that connect opposite RF electrodes in both layers. Bottom layer is dark gray. Alternatively, opposing control electrodes can be connected. (b) Perspective view.

3 Layered Construction

A straightforward approach to incorporating microfabrication into trap construction is to use multi-layer processing to reproduce the quadrupole geometry on a smaller scale. Although the standard four-electrode design may be implemented with two electrode layers and an intervening insulating layer as in [9] (see Fig. 2c), this construction is not adequate for tee junctions and other complicated patterns. However, four-junction crosses can be made with a slight modification to the two-layer design. Figure 3 shows the proposed modification to a standard two-layer cross (the intersection of two linear traps, each of which is composed of two conducting layers) such that charged particles can be trapped in the intersection region. By connecting the RF electrodes (or alternatively the control electrodes) with diagonal bridges, a trapping minimum can be created at the cross's center. Variation of the potentials on control electrode segments (not shown) allows movement of charged particles through the cross region into any of the branches while maintaining a stable minimum at every point along the trajectory.

As an alternative to the two-layer realization of the four-rod design, a deformation of the quadrupole to six electrodes in a three-layer geometry allows more flexibility with trap layout (see Fig. 4a) [3, 27]. This construction requires three conducting layers sandwiching two insulating layers. A potential problem with this approach may be the difficulty of fabrication using standard microfabrication techniques. The insulating layers must be low RF-loss materials, and ideally, they must have a thickness approximately equal to the lateral electrode spacing. This dimension must be $\gtrsim 10 \mu\text{m}$ to allow for optical access. For aspect ratios $\gamma \equiv \text{width/height}$ (Fig. 4) between 1 and 15, the depth of the trap, due to the nearby local maxima above and below the trapping region, scales as approximately $\gamma^{-2.01}$ for a constant trap width (this assumes conductors rectangular in cross-section with thickness approximately 0.02 times

the trap width). Similarly, the secular frequency obtained for a constant applied potential at a fixed frequency with the same electrode geometry scales as approximately $\gamma^{-0.93}$ in this range of aspect ratios.

These scaling relations were determined numerically by means of pseudopotential calculations. This and the other simulations referred to below relied on numerical relaxation to determine the electrostatic potential of an electrode geometry. The field was determined from the potential, and the pseudopotential was calculated as in Eq. 1.

The scaling relations determined for the three-layer constant-width geometry suggest that the insulating layers should be quite thick, and to facilitate fabrication, methods are required for either deposition or deep etching of thick layers. This limits the materials and processes that can be used. Typical materials such as silicon and gallium arsenide lead to significant RF loss; aluminum gallium arsenide, which can be grown epitaxially on gallium arsenide, has been suggested as an insulator [5], however. Thick layers of low-loss materials such as sapphire, alumina, and quartz are difficult to deposit and etch. Lateral extension of the center electrodes in the three-layer geometry beyond the upper and lower electrodes towards the center of the trap [13] strengthens and deepens the trap, but fabrication of such a structure may require more etch steps and hence may become more difficult.

The problems with designs of high aspect ratio ($\gamma \gg 1$) are not as pronounced for the standard four-electrode configuration [4, 5, 9], and small versions of this type of trap may be built using multi-layer microfabrication. Two conducting layers and one insulating layer, each as thin as a few micrometers, would be suitable for a trap.

4 Surface Geometry

Deformation of the standard quadrupole geometry electrodes into a plane preserves a quadrupolar field for a wide range of parameters while also providing an avenue to more straightforward fabrication. The most obvious planar deformation is to move one control electrode and one RF electrode into the plane of the remaining two electrodes, such that the electrodes are of alternating potential (RF, control, RF, and control), as shown in Fig. 4b. The trap axis remains in approximately the same position, above and between the center two electrodes (there is another trap axis symmetrically opposite this one, beneath the electrodes, but this axis will typically reside within the substrate). This “four-wire” geometry appears promising, but making connections to the segments of both control electrodes requires multi-layer processing or the use of vias through the substrate. Alternatively the outer RF and control electrodes could be segmented and different control potentials applied, but this is complicated by the practical difficulty of applying control potentials to the electrodes without affecting application of the RF potential. An alternative is the segmentation of only the outer control electrode for axial confinement. The asymmetry in this configuration requires adjustment of the other (nonsegmented) control electrode to compensate for the lateral field due to the single segmented electrode. In addition, structures such as tee junctions may be difficult to construct with four wires in this configuration.

To alleviate these problems with the four-wire planar geometry, the four-rod quadrupole can instead be deformed into a “five-wire” design, in which the center and outer electrodes are maintained at RF ground, and the remaining two electrodes support an RF potential (see Fig. 4c). In this geometry, the trap axis is above (and below) the center electrode, and the

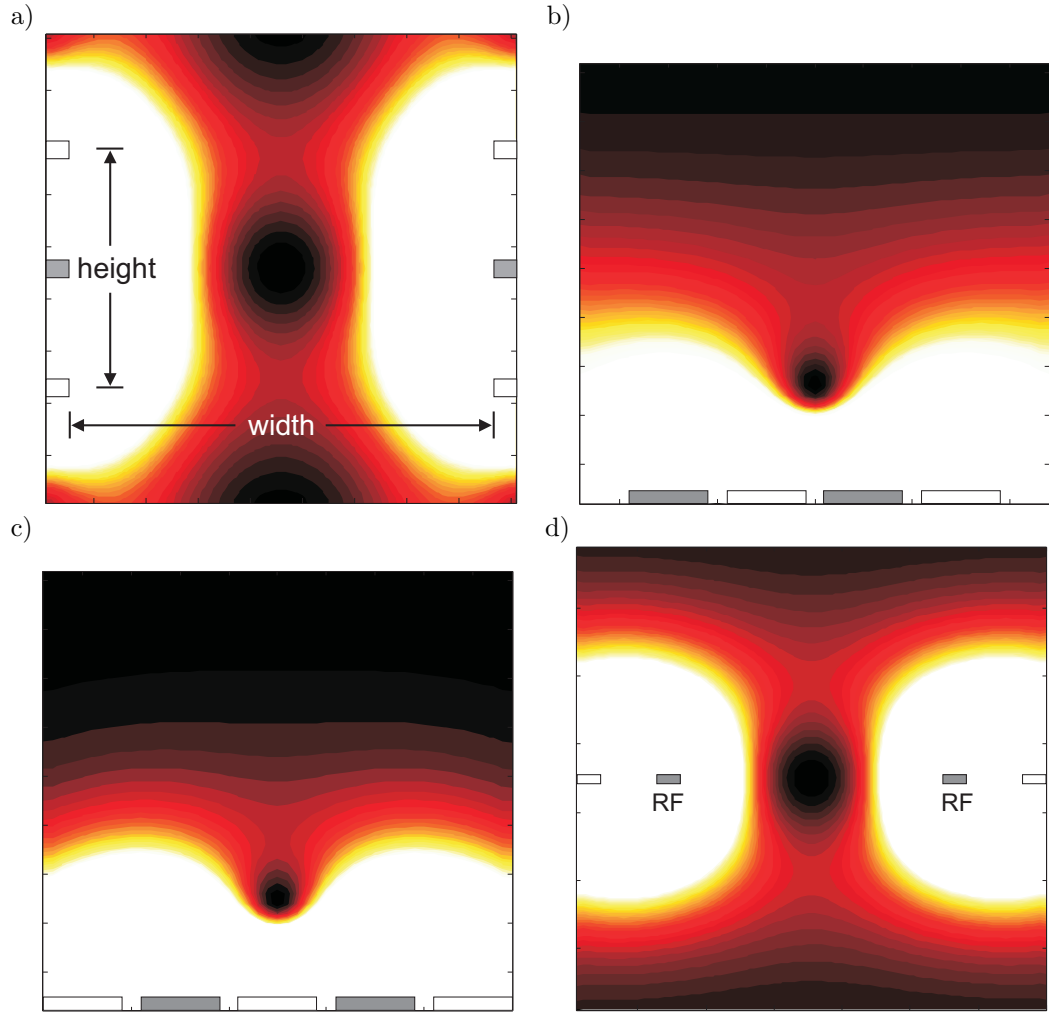


Fig. 4. Radial pseudopotential contours (looking down the trap axis) for four linear RF-trap geometries. Colors from black to white indicate low to high pseudopotential, respectively. For clarity, contours are not shown for pseudopotential values above an arbitrary maximum. An RF potential is applied to the gray electrodes, and the white electrodes are held at RF ground. For engineering simplicity, it would usually be more convenient to apply the control potentials to the RF-ground electrodes. For each geometry, secular frequencies f_i and trap depths u_{\max} , normalized to the values for a two-layer quadrupole with an aspect ratio (equal to the width over the height) $\gamma = 1$ (Fig. 2c) with identical drive frequency, RF potential amplitude, and ion mass, are listed. These values are for identical distance d from the trap axis to the nearest electrode surface and for an electrode thickness of $0.10d$, and they were calculated numerically as described in the text. (a) A three-layer geometry with $\gamma = 1.8$. For this geometry $f_i = 0.52$ and $u_{\max} = 0.078$. For the simulation of this design, the electrodes were taken to extend semi-infinitely in the lateral directions. (b) A planar geometry with trapping axis offset from the plane of the electrodes. For this geometry $f_i = 0.34$ and $u_{\max} = 0.017$. (c) A similar trapping potential produced with a surface geometry made up of five electrodes. For this geometry $f_i = 0.30$ and $u_{\max} = 0.010$. (d) A planar geometry with trapping minimum in the plane of the electrodes. For this geometry $f_i = 0.32$ and $u_{\max} = 0.051$.

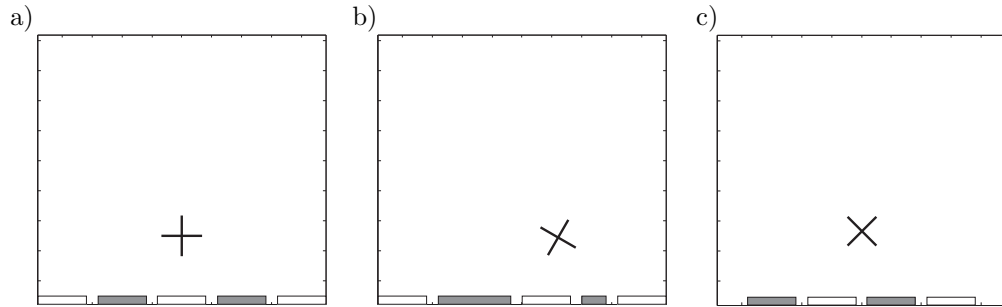


Fig. 5. Trap principal axes directions for three different surface trap configurations. The third principal axis is perpendicular to the page and not shown. The transverse axes directions are depicted by two orthogonal lines at the trap axis location and are determined by static potentials applied between segments of the gray (RF) and white (control) electrodes. The axes directions are close to those shown for a large range of control voltages (relative to the RF potential amplitude). (a) Five-wire geometry, all electrodes of equal width. (b) Five-wire geometry, RF electrode widths altered. (c) Four-wire geometry.

two outer electrodes can be segmented for longitudinal confinement and control. There may be advantages for ion separation if the center electrode is segmented (see below), but making connections to the segments would require multi-layer processing or through-layer vias, a complication we do not consider here. As the five-wire design obeys a mirror symmetry through the plane containing the center electrode and perpendicular to the substrate plane, tee junctions are straightforward to construct (see Fig. 1).

In a linear trap, an added static potential, as opposed to the pseudopotential, defines the two radial major trap axes, because the pseudopotential is cylindrically symmetric near the center of the trapping region (see Eq. 2 and Fig. 2b). In the designs discussed here, the static potential, acting alone, leads to a maximally trapping direction and a perpendicular, maximally anti-trapping direction in the x - y plane (perpendicular to the long direction); these two directions define the major trap axes for the combination of the static potential and the RF pseudopotential. By symmetry, the standard five-wire design (Fig. 4c) provides a static potential with major trap axes perpendicular and parallel to the substrate (the third axis in a linear trap will be along the long dimension of the wires) as in Fig. 5a. By changing the relative lateral sizes of the electrodes, the major axes of the trap may be rotated (for instance, if the width of one of the RF electrodes is increased by half its width, and the width of the other RF electrode is decreased by the same amount, the principal axes rotate by 30°) as depicted in Fig. 5b. This allows Doppler-cooling laser beams whose wavevectors are parallel to the substrate to cool the ions' motion in both radial-axis directions [28], that is, the ions will not be heated through recoil along any of the principal axes. This might be necessary as beams with wavevectors nonparallel to the surface may produce significant amounts of scattered light. The orientation of the trap principal axes in the four-wire surface geometry is approximately $\pm 45^\circ$ from horizontal (parallel to the substrate) for a large range of electrode potentials and thus allows laser-cooling along all three axes with a beam parallel to the surface (see Fig. 5c).

A potential benefit of the planar electrode configuration is that the location and strength of the trapping region may be altered by varying the electrode structure in one dimension

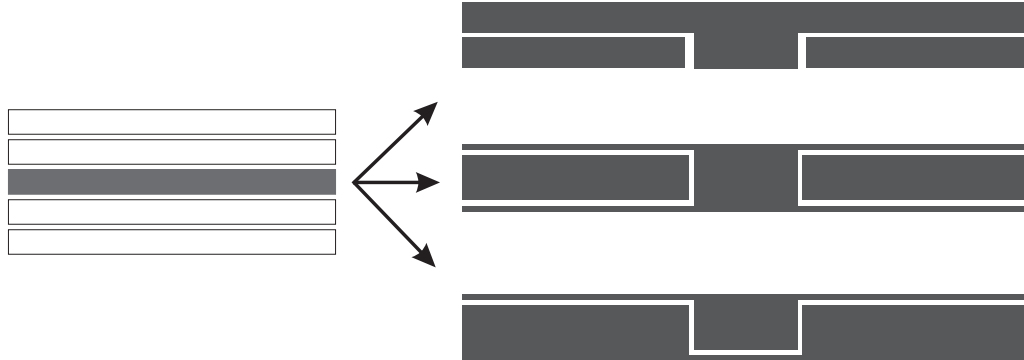


Fig. 6. Three different options for layout of composite center control electrode in planar five-wire geometry to allow for efficient separation of ions. A similar layout can be used in the four-wire geometry, as well. Electrode structure appears as viewed from above the substrate. The top two versions split the center electrode into three electrodes: the effect of the continuous electrode in each case can be partially canceled by the shorter electrodes everywhere but in the separation region. In the bottom version, the center electrode is split longitudinally in two continuous electrodes, and the separation potential can be applied to the electrode with greater extent in the separation region. The field due to this electrode is nearly canceled outside this region by the other, relatively wider electrode.

(the lateral direction) only. Through overall scaling of the electrode size and spacing, the distance from the trap axis to the electrodes and substrate may be controlled so that the effects of surface proximity on ion heating [29] may be studied (see Sec. 7). This distance can be changed continuously along the length of the electrodes, in effect creating a trapping region for any desired surface-ion separation distance.

Another possible benefit of the surface geometry is that it may facilitate ion separation [9, 30]. Two ions or groups of ions in the same longitudinal trapping region may be separated by raising the potential of an electrode near the center of the trapping region. As this potential is raised, the ions' motional frequencies necessarily drop as the external potential becomes flat. The minimum motional frequency during the separation increases as the splitting electrode's size and the ions' proximity to this electrode become smaller. According to numerical simulation, the minimum frequency ω_{\min} is approximately proportional to $1/L$ (where L is the distance from the ions to the nearest control electrode) in agreement with [7]. We want to keep this minimum frequency as high as possible, both to minimize kinetic excitation of the ions' motional modes and motional heating due to stray fluctuating charges, and to maximize the speed at which the operations can be performed [7, 9]. In the five-wire geometry, the center electrode will be nearest to the ions (in the four-wire geometry, the inner control electrode will be at a comparable distance from the trap axis for a similarly sized geometry). This central electrode may be split into several segments, some with greater extent in the longitudinal or lateral directions (see Fig. 6). Potentials applied to a subset of these electrodes may be tuned to nearly cancel the field due to the remaining electrodes everywhere but in a small region where the ions will be separated. The close proximity of the electrode can lead to very efficient ion separation.

Another possible four-wire configuration that will create a quadrupole field is a pair of

parallel RF electrodes flanked by two outer RF-ground electrodes. Here the trap axis will lie between the two RF electrodes, as shown in Fig. 4d. This places the trap very close to the substrate unless a slot is etched through it between these two electrodes. It also places the RF electrodes between the trap axis and the control electrodes, limiting the effectiveness of the control electrodes in the longitudinal direction. An alternative is the use of freestanding wires for this design, with separate electrodes for axial confinement.

5 Strength and Depth of Surface-Electrode Geometry Trap

The trap frequencies in both surface trap designs can be made comparable to those in the standard quadrupole of similar size. All else being equal, the radial frequencies are approximately one sixth to one third (depending on exact electrode shape) of those in a standard four-rod quadrupole of similar size (see Appendix A for a comparison to a thin-wire surface design). However, the surface traps suffer from a much shallower trap depth. There is a local maximum in the pseudopotential at a distance proportional to and of the same order as d above the trap axis in both cases (see Figs. 4b, 4c, or Fig. A.1), and the depth of the trap (defined by this maximum) is smaller by a factor of approximately 30 to 200 than the depth of the standard quadrupole trap, depending on electrode shape. Typical trap depths for the four-rod quadrupole design are on the order of a few electron volts (1 eV is approximately equivalent to 12 000 K); a trap depth significantly less than this is adequate once the ion is trapped and cooled, but the initial loading efficiency could be compromised due to the small trap depth. Ions are typically produced by means of electron-impact ionization or photoionization of a thermal neutral atomic source. Some typically trapped atomic species, such as beryllium, must be produced from an evaporation source at a temperature of ~ 1000 K. One will need to depend on the low-energy tail of the Boltzmann distribution of atom kinetic energies for trappable atoms if the trap depth is low. A possible solution is the integration of a load/reservoir trap of a more standard design. This trap would be more efficient for loading ions, and a large number can be obtained and held until they are needed, at which time they can be shuttled into the surface trap for computational purposes. Also, lost ions (due to chemical reaction or background-gas collisions) can be replaced with ions from this reservoir. Numerical simulations suggest that a smooth crossover between the two trap geometries is feasible.

The pseudopotential trap depth in the surface designs can be increased by adjusting the static potential used to bring about axial confinement. The static potential due to voltages applied to the segmented electrodes is typically trapping in the direction of one of the radial principal axes and antitrapping in the direction of the other. Calculations suggest that variation of the principal axes angles (as mentioned above) and the magnitude of the control voltages can deepen the trap by factors of about 2.

Although current trap designs must be reduced in size to scale to large numbers of qubits, there may be an ultimate limit to how small any linear RF Paul trap can be made. Calculations (see Appendix B) suggest that scaling beyond an ion-electrode distance of tens of nanometers may become impossible due to reduced trap depth, even using a standard quadrupole trap.

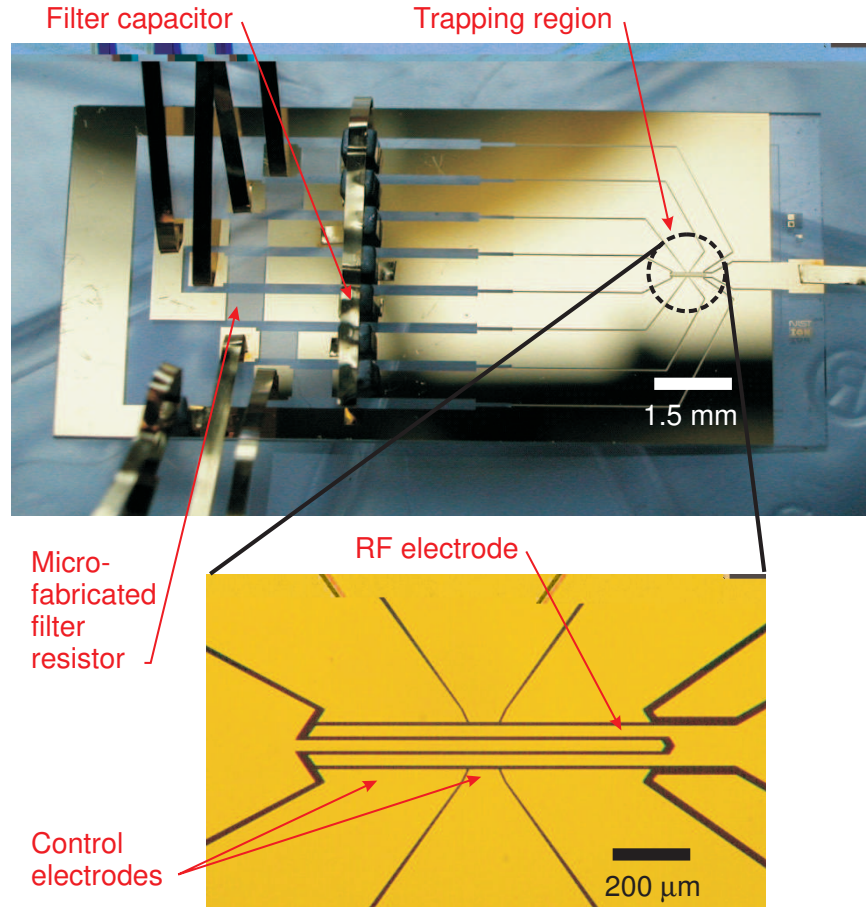


Fig. 7. Micrographs of a five-wire, one-zone linear trap fabricated of gold on fused silica. The top figure is an overview of the trap chip showing contact pads, onboard passive filter elements, leads, and trapping region. Substrate dimensions are $10\text{ mm} \times 22\text{ mm} \times 500\text{ }\mu\text{m}$. The lower image is a detail of the trapping region indicated by the dotted ring in the top figure. The substrate material appears dark-colored in the lower image.

6 Implementation

Utilizing the techniques developed for the microelectronics industry, ion traps of planar geometry can be constructed in only a few fabrication steps. The basic structure can be made by means of patterned metal deposition onto an insulating substrate. Photolithography or electron beam lithography can be utilized to define the electrodes. This method is similar to that used for neutral atom optics and atom guides on chips [31, 32, 33, 34, 35, 36, 37]. An ion trap structure fabricated in this manner is shown in Fig. 7.

Calculations suggest that a trap of this construction will be capable of trapping ions approximately $50\text{ }\mu\text{m}$ from the chip surface. Secular frequencies will be in the 10 MHz range for an applied RF potential of amplitude 100 V at 100 MHz. Control electrode potentials of a few volts will lead to axial frequencies in the few megahertz range. The dissipation in the

trap can be modeled as a resistor representing the leads in series with the trap capacitance and its equivalent series resistance, which is proportional to the dielectric loss. In this case, the dissipated power will be $P = I_{\text{RMS}}^2(R_{\text{Lead}} + R_{\text{ESR}}) = (C\Omega V_{\text{RMS}})^2(R_{\text{Lead}} + \tan \delta / (C\Omega))$, where I_{RMS} is the root-mean-square RF current, R_{Lead} is the total lead resistance, $R_{\text{ESR}} = \tan \delta / (C\Omega)$ is the equivalent series resistance of the capacitance C between the RF and RF-grounded electrodes, $V_{\text{RMS}} = V_0/\sqrt{2}$, and $\tan \delta$ is the loss due to the substrate. For the trap parameters listed above, lead resistance totalling 1Ω , a total trap capacitance of 3 pF , and a loss tangent of 0.0004 (for fused silica), the dielectric loss is slightly less than the resistive loss, and the RF power dissipation in the trap in Fig. 7 is 20 mW (see Appendix C for a list of material and electrical properties for typical and suggested substrates). The values for the lead resistance and capacitance are correct for the structure shown in Fig. 7, but will vary with the overall size of the trap and the number of electrodes.

The control electrodes require RF grounding capacitors, and it is desirable to filter the external control potentials with low-pass RC filters. We have typically accomplished this with a separate board containing surface-mounted components and another set of connections between this “filter board” and the trap [9]. Typical values for the resistor and capacitor are approximately $1 \text{ k}\Omega$ and 1 nF , respectively, leading to a high frequency roll-off of approximately 160 kHz . With these components, control electrode voltages can be changed such that ions can be transported in segmented traps in tens of microseconds. Future traps may need to employ filters with higher roll-off frequencies so that ions can be transported more quickly.

Since the fabrication procedure for the planar trap is relatively straightforward, passive filter elements may be incorporated directly on the trap chip. The chip shown in Fig. 7 contains a low-pass filter on each control electrode lead consisting of a resistor and capacitor to ground. The resistor is a long, thin meander wire of the same metal as the trap electrodes, and the capacitor is a separate surface-mount component. Capacitors could be made during the microfabrication, as a pair of parallel plates with silicon dioxide as an insulator. This construction adds two thin-film depositions to the fabrication.

One concern with this design is the proximity of insulating surfaces between the electrodes that can hold charge and perturb the trapping field in the vicinity of the ions. In the proposed surface electrode configuration, the spaces between the electrodes will be bare insulator, and charges on these surfaces may be problematic. To minimize the effect of charging, trenches that undercut the metal layer may be etched into the substrate between the electrodes; if the depth of the trenches is more than a few times the width of the space between the electrodes, the (possibly charged) insulator’s influence on the field at the ion will be suppressed. Toward this end, the insulator may be etched via a wet chemical etch or a reactive ion etch after an additional lithographic masking step. An alternative is to electroplate the electrodes to a height more than a few times the inter-electrode spacing to accomplish the same effect.

The choice of materials used in the construction of these traps is important as the electrode surface can influence vibrational-mode heating of the ions (see next section), and the substrate supporting these electrodes must have low RF loss. The planar trap fabrication, as described above, may incorporate many different metals, as evaporation, sputtering, and electroplating can employ a wide variety of materials. Gold’s relative surface cleanliness makes it a reasonable choice, although refractory metals or other noble metals that do not support significant surface oxides may also be investigated. Similarly, there are many choices for

substrate material, as the fabrication method requires only a relatively smooth surface and reasonable adhesion properties to metal films. Fused silica and quartz have the added benefits of low RF loss and some ability to be etched. Other options include aluminum nitride, sapphire, alumina, and diamond, although etching difficulties with the latter three materials may imply use only in the electroplating procedure. Doped silicon may also be used as an electrode material, and the electrodes can be defined using through-wafer reactive ion etching (ions have been trapped in a doped silicon structure of the standard quadrupole design [38]). There would be no insulator near the trapped ion's position, and optical access may be provided through etched gaps between the electrodes in the planar structure. The doped silicon electrodes can be supported by a glass substrate (away from the trapping region) attached by means of anodic wafer bonding [39]. Gallium-arsenide and aluminum-gallium-arsenide combinations could also be good electrode choices [40], and in a separate design, silicon carbide has been suggested to provide structural support for metallic electrodes [41].

The effect of a dielectric substrate on the trapping fields above the surface-mounted electrodes must be considered, as many of the suggested materials have relative dielectric constant $\epsilon > 10$. The field in the dielectric will be modified, and at the dielectric-vacuum interface, a component of the electric field will be discontinuous. This may lead to modification of the field at the location of the ions. Simulations of the surface geometry with a substrate with $\epsilon = 1$ (which is the case for all the field simulations discussed above) have been compared to similar simulations with a substrate with $\epsilon = 10$. For gaps between the electrodes as big as 1/4 the width of the electrode segments, the difference in the electric field in and near the trapping region is on the 1 % level. This difference will be smaller for the smaller relatively-sized gaps employed in current designs, but it could be significant in the limit of thin wire-electrodes separated by large open regions of the substrate surface.

We also note that the proximity of the electrodes to the ions possible with the surface-electrode design suggests the possibility of performing single-qubit rotations by use of microwaves delivered to the ions via the trap structure. A subset of the planar trap wires could make up a waveguide or cavity for long-wavelength radiation. Unlike coherent operations performed via two-photon stimulated-Raman transitions, single-bit rotations brought about using microwaves are practically immune to the effects of spontaneous emission [2, 42]. Such manipulation of electronic hyperfine levels using near-field microwave radiation has been proposed for ion traps [42] and neutral-atom chip-traps [43].

7 Heating Studies

Heating of a trapped ion's motional modes can occur from thermal electronic noise in the metal of the electrodes (or in resistive elements connected to these electrodes), fluctuating patch potentials on the surfaces of the electrodes, and perhaps other unknown sources. Each creates heating rates that scale as some power of the distance between the ion and the electrodes [29, 44]. The planar trap described above offers a method to study the effects of this type of heating and to verify the scaling with distance.

Heating due to Johnson noise in the electrodes will cause fluctuations in the field at the ion, and the heating rate due to these fluctuations is expected to scale as d^{-3} for $d \ll \delta_S$, where d is the distance from ion to electrode and δ_S is the skin depth of the electrode metal [44]. For $d \gg \delta_S$, the heating rate should scale as d^{-2} [29, 44, 45]. Heating due to fluctuating surface

patch potentials may scale more steeply. Ref. [29] indicates a scaling of d^{-4} if the size of the patches is smaller than d .

The geometry described above can easily be made smaller than most current designs, and hence the trapped ions can be placed much closer to the electrodes than in previous traps. The spacing and size of the planar electrodes may be changed as a function of distance along the trap axis, therefore varying the ion-electrode distance over a wide range on one chip. Tests of the scaling of these heating rates is very important as traps become smaller. The requirements for sympathetic cooling and constraints on ion motion must be determined, and these depend crucially on the heating rate.

As in other small ion traps, there is a concern with accumulated films of the to-be-trapped material on the trap electrodes. There has been some evidence that this material can lead to ion motional-state heating at anomalously high rates [9, 29]. In light of the attainable proximity of ions to the electrodes in the surface geometry, this may be even more important in this case. Large-scale designs may require separate loading and experimental zones as has been implemented in previous designs [46].

Charging of trap or structural components due to electrons from impact ionization may also lead to unpredictable heating or ion-trapping behavior. A separate loading zone can alleviate this problem if the experimental zone is sufficiently far away. Alternately, photoionization may be employed if suitable radiation sources are available; the usefulness of this technique is ion-species-specific, however.

8 Remarks

We have explored the feasibility of some different linear ion-trap electrode geometries in the context of multiplexed trapped-ion quantum information processing. Both four- or five-wire surface geometries comprising metal deposited on an electrically insulating substrate can maintain a trap axis above the chip and are promising for scaling ion systems toward large-scale quantum information processing. The fabrication of such trap chips is straightforward, and allows for rapid turnaround in design and construction as well as the inclusion of complicated electrode patterns without additional fabrication effort. This design also allows for the construction of traps much smaller than those currently in use, a necessity for faster ion-qubit logic operations. Ion motional heating, which may ultimately limit the size and speed of these ion trap arrays, may also be explored in designs of this type. Experiments whose goal is to trap atomic ions in this type of electrode structure are currently underway. Planar traps of similar design have been demonstrated recently for macroscopic charged particles [47]. We have also suggested a modification of a two-layer design to allow crosses at the intersection of two linear traps to facilitate two-dimensional ion-trap arrays.

After submission of this manuscript, a publication suggesting a planar Penning-trap design came to our attention [48]. In contrast to the RF Paul trap designs discussed here, Penning traps use combined static electric and magnetic fields to trap charged particles in three dimensions.

Acknowledgements

DJW thanks M. Prentiss (Harvard University) for the suggestion of planar electrode geometries. The authors thank J. Koelemeij and S. Seidelin for helpful comments on the manuscript.

This work was supported by the U.S. National Security Agency (NSA) and the Advanced Research and Development Activity (ARDA). This manuscript is work of the National Institute of Standard and Technology and is not subject to U.S. copyright.

References

1. J. I. Cirac and P. Zoller, "Quantum Computations with Cold Trapped Ions," *Phys. Rev. Lett.* **74**, 4091–4094 (1995).
2. D. J. Wineland *et al.*, "Experimental issues in coherent quantum-state manipulation of trapped atomic ions," *J. Res. Natl. Inst. Stand. Technol.* **103** (3), 259–328 (1998).
3. D. Kielpinski, C. Monroe, and D. J. Wineland, "Architecture for a Large-Scale Ion-Trap Quantum Computer," *Nature* **417**, 709–711 (2002).
4. D. Leibfried, *et al.*, "Towards quantum information with trapped ions at NIST," *J. Phys. B* **36**, 599–612 (2003).
5. M. J. Madsen, W. K. Hensinger, D. Stick, J. A. Rabchuk, and C. Monroe, "Planar ion trap geometry for microfabrication," *Appl. Phys. B* **78**, 639–651 (2004).
6. C. F. Roos *et al.*, "Control and Measurement of Three-Qubit Entangled States," *Science* **304**, 1478 (2004).
7. J. P. Home and A. M. Steane, "Electric octopole configurations for fast separation of trapped ions," arXiv:quant-ph/0411102 (2004).
8. D. Leibfried *et al.*, "Experimental demonstration of a robust, high-fidelity geometric two ion-qubit phase gate," *Nature* **422**, 412–415 (2003).
9. M. A. Rowe, *et al.*, "Transport of quantum states and separation of ions in a dual RF ion trap," *Quant. Inf. Comput.* **2**, 257–271 (2002).
10. H. Rohde *et al.*, "Sympathetic ground-state cooling and coherent manipulation with two-ion crystals," *J. Opt. B Quantum Semiclassical Opt.* **3**, S34–S41 (2001).
11. B. B. Blinov *et al.*, "Sympathetic Cooling of trapped Cd⁺ isotopes," *Phys. Rev. A* **65**, 040304 (2002).
12. M. D. Barrett *et al.*, "Sympathetic cooling of ⁹Be⁺ and ²⁴Mg⁺ for quantum logic," *Phys. Rev. A* **68**, 042302 (2003).
13. C. A. Schrama, E. Peik, W. W. Smith, and H. Walther, "Novel miniature ion traps," *Opt. Commun.* **101**, 32–36 (1993).
14. H. C. Nägerl, W. Bechter, J. Eschner, F. Schmidt-Kaler, and R. Blatt, "Ion strings for quantum gates," *Appl. Phys. B* **66**, 603–608 (1998).
15. Ralph G. DeVoe, "Elliptical ion traps and trap arrays for quantum computation," *Phys. Rev. A* **58**, 910–914 (1998).
16. P. A. Barton *et al.*, "Measurement of the lifetime of the $3d^2D_{5/2}$ state in ⁴⁰Ca⁺," *Phys. Rev. A* **62**, 032503 (2000).
17. G. R. Guthöhrlein, M. Keller, K. Hayasaka, W. Lange, and H. Walther, "A single ion as a nanoscopic probe of an optical field," *Nature* **414**, 49–51 (2001).
18. L. Hornekaer, N. Kjærgaard, A. M. Thomsen, and M. Drewsen, "Structural Properties of Two-Component Coulomb Crystals in Linear Paul Traps," *Phys. Rev. Lett.* **86**, 1994–1997 (2001).
19. D. J. Berkeley, "Linear Paul trap for strontium ions," *Rev. Sci. Instrum.* **73**, 2856–2860 (2002).
20. W. Paul, "Electromagnetic traps for charged and neutral particles," *Rev. Mod. Phys.* **62**, 531–540 (1990).
21. E. Fischer, "The three dimensional stabilizing of charged particles in a quadrupole field," *Z. Phys.* **156**, 1–26 (1959).
22. R. F. Wuerker, H. Shelton, and R. V. Langmuir, "Electrodynamic Containment of Charged Particles," *J. Appl. Phys.* **30**, 342–349 (1959).
23. H. G. Dehmelt, "Radiofrequency spectroscopy of stored ions I: Storage," *Adv. Atom. Mol. Phys.* **3**, 53 (1967).

24. P. K. Ghosh, *Ion Traps* (Clarendon Press, Oxford, 1995).
25. J. D. Prestage, G. J. Dick, and L. Maleki, “New ion trap for frequency standard applications,” *J. Appl. Phys.* **66**, 1013 (1989).
26. M. G. Raizen, J. M. Gilligan, J. C. Bergquist, W. M. Itano, and D. J. Wineland, “Ion crystals in a linear Paul trap,” *Phys. Rev. A* **45**, 6493 (1992).
27. L. Deslauriers, *et al.*, “Zero-point cooling and low heating of trapped $^{111}\text{Cd}^+$ ions,” *Phys. Rev. A* **70**, 043408 (2004).
28. W. M. Itano and D. J. Wineland, “Laser cooling of ions stored in harmonic and Penning traps,” *Phys. Rev. A* **25**, 35–54 (1982).
29. Q. A. Turchette *et al.*, “Heating of trapped ions from the quantum ground state,” *Phys. Rev. A* **61**, 063418 (2000).
30. M. D. Barrett *et al.*, “Deterministic quantum teleportation with atomic qubits,” *Nature* **429**, 737–739 (2004).
31. E. A. Hinds and I. G. Hughes, “Magnetic atom optics: mirrors, guides, traps, and chips for atoms,” *J. Phys. D: Appl. Phys.* **32**, R119–R146 (1999).
32. D. C. Lau *et al.*, “Magnetic mirrors with micron-scale periodicities for slowly moving neutral atoms,” *J. Opt. B Quantum Semiclassical Opt.* **1**, 371–377 (1999).
33. R. Folman *et al.*, “Controlling Cold Atoms using Nanofabricated Surfaces: Atom Chips,” *Phys. Rev. Lett.* **84**, 4749–4752 (2000).
34. N. H. Dekker *et al.*, “Guiding neutral atoms on a chip,” *Phys. Rev. Lett.* **84**, 1124–1127 (2000).
35. J. Reichel, W. Hänsel, P. Hommelhoff, and T.W. Hänsch, “Applications of integrated magnetic microtraps,” *Appl. Phys. B* **72**, 81–89 (2001).
36. D. Müller *et al.*, “Magnetic switch for integrated atom optics,” *Phys. Rev. A* **63**, 041602 (2001).
37. B. Lev, “Fabrication of micro-magnetic traps for cold neutral atoms,” *Quant. Inf. Comput.* **3**, 450–464 (2003).
38. J. Britton *et al.*, unpublished.
39. D. Kielpinski, *Entanglement and decoherence in a trapped-ion quantum register*, Ph. D. thesis, Department of Physics, University of Colorado, Boulder (2001).
40. C. Monroe, private communication.
41. A. Ben-Kish and R. Folman, private communication.
42. F. Mintert and C. Wunderlich, “Ion-Trap Quantum Logic Using Long-Wavelength Radiation,” *Phys. Rev. Lett.* **87**, 257904 (2001).
43. P. Treutlein, P. Hommelhoff, T. Steinmetz, T. W. Hänsch, and J. Reichel, “Coherence in Microchip Traps,” *Phys. Rev. Lett.* **92**, 203005 (2004).
44. C. Henkel, S. Pötting, and M. Wilkens, “Loss and heating of particles in small and noisy traps,” *Appl. Phys. B* **69**, 379–387 (1999).
45. D. J. Wineland and H. G. Dehmelt, “Principles of the stored ion calorimeter,” *J. Appl. Phys.* **46**, 919–930 (1975).
46. J. Chiaverini *et al.*, “Recent experiments in trapped-ion quantum information processing at NIST,” Proceedings of the 2005 International Conference on Coherent and Nonlinear Optics (ICONO 2005), St. Petersburg, Russia, to be published in the Proceedings of the SPIE (2005).
47. I. L. Chuang, private communication.
48. S. Stahl *et al.*, “A planar Penning trap,” *Eur. Phys. J. D* **32**, 139–146 (2005).
49. G. R. Janik, J. D. Prestage, and L. Maleki, “Simple analytic potentials for linear ion traps,” *J. Appl. Phys.* **67**, 6050–6055 (1990).
50. R. Gomer, *Field Emission and Field Ionization* (Harvard University Press, Cambridge 1961).
51. L. Tian and P. Zoller, “Coupled Ion-Nanomechanical Systems,” *Phys. Rev. Lett.* **93**, 266403 (2004).

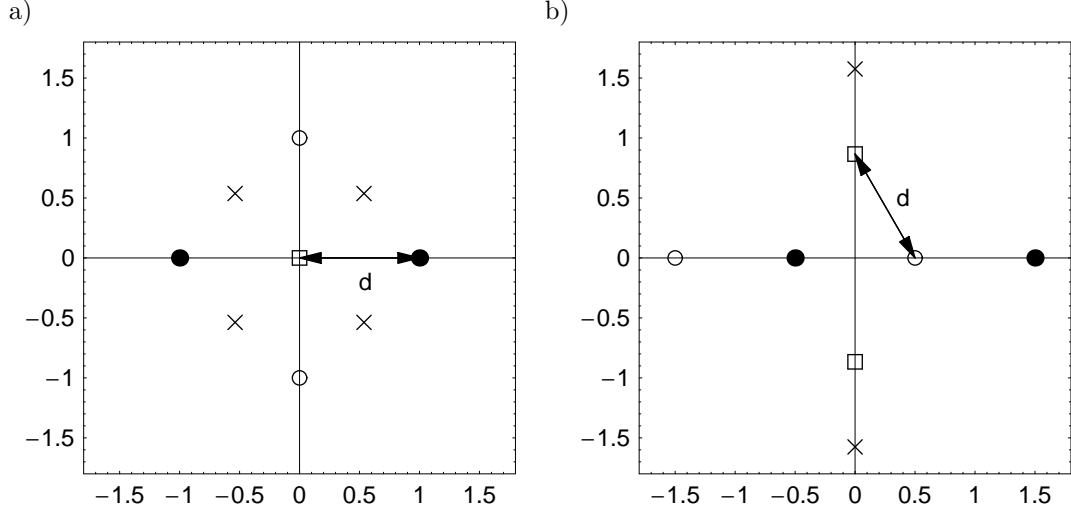


Fig. A.1. Complex plane showing the locations of positive line charges (‘•’), negative line charges (‘◦’), trap minima (‘◻’), and trap local maxima (‘×’). (a) Standard quadrupole geometry. (b) Four-wire surface electrode geometry.

Appendix A: Analytic comparison of standard quadrupole and four-wire surface geometries

To compare the pseudopotential (in two dimensions) of the four-wire surface trap to that of the standard quadrupole, complex variables can be used (here we follow the method of [49]). In the following comparison we assume identical RF potentials applied to electrode structures trapping particles of identical mass and charge, and we assume a uniform static axial potential. We first calculate the pseudopotential of systems of line charges as a limiting case of the typical rod or wire conductors and then discuss finite-size effects. In general, the results are directly applicable to the case where the lateral electrode dimensions are much smaller than their separation, but they give some qualitative insight for the case proposed above, in which the spacings between electrodes can be small.

The complex potential due to a positive line charge with charge per unit length λ located at $z = x + iy = z_0$ is $w(z) = -(\lambda/2\pi\epsilon_0)\ln(z - z_0)$. The real part of this expression is the electric potential. The electric-field components E_x and E_y can be determined by means of the relation $dw/dz = -E_x + iE_y$. The potential $w_q(z)$ for a standard quadrupole trap would consist of positive line charges at $z = \pm 1$ and negative line charges at $z = \pm i$ (see Fig. A.1a), which is $w_q(z) = \ln [(z^2 + 1)/(z^2 - 1)]$ (here and below, we let $\lambda/2\pi\epsilon_0 = 1$). Since the pseudopotential is proportional to the square of the electric field, we calculate the quantity

$$\Upsilon_q(z) = \left| \frac{dw_q}{dz} \right|^2 = \frac{16|z|^2}{|z^4 - 1|^2}. \tag{A.1}$$

The function $\Upsilon_q(z)$ is not in standard units but is suitable for comparisons between geometries. The pseudopotential of the quadrupole can be seen to have a minimum at the origin, $\Upsilon_q(0) =$

0. This is the trap axis, where the distance d from the axis to the nearest line charge is equal to 1. The second spatial derivative of the pseudopotential (the curvature) at this point can be found to be $\frac{d^2\Upsilon_q(z)}{dz^2}|_{z=0} = 32$. There are four local maxima at the points $z = z_m = \pm \frac{1}{\sqrt{2\sqrt{3}}} \pm i \frac{1}{\sqrt{2\sqrt{3}}}$ with $\Upsilon_q(z_m) = 3\sqrt{3}$. The minimum and local maxima are labeled in Fig. A.1a.

Applying the same analysis to a four-wire surface geometry for positive line charges at the points $z = -1/2$ and $z = 3/2$ and negative line charges at the points $z = -3/2$ and $z = 1/2$ (see Fig. A.1b), we obtain the complex potential

$$w_s(z) = \ln \frac{(z - \frac{1}{2})(z + \frac{3}{2})}{(z + \frac{1}{2})(z - \frac{3}{2})}. \quad (\text{A.2})$$

This gives a pseudopotential function (now switching to x and y)

$$\Upsilon_s(x, y) = \frac{64 \left(16x^4 + (3 - 4y^2)^2 + 8x^2(3 + 4y^2) \right)}{\left((1 - 2x)^2 + 4y^2 \right) \left((3 - 2x)^2 + 4y^2 \right) \left((1 + 2x)^2 + 4y^2 \right) \left((3 + 2x)^2 + 4y^2 \right)}. \quad (\text{A.3})$$

This is not particularly revealing, but differentiating, one finds two pseudopotential minima $\Upsilon_s(0, \pm\sqrt{3}/2) = 0$, which define the trap axes above and below the surface, each a distance $d = 1$ from the nearest line charge. The pseudopotential curvature at this point is $8/3$, which is $1/12$ of the curvature in the standard quadrupole case, leading to radial secular frequencies $\frac{1}{2\sqrt{3}} \approx 0.29$ times as large as in the standard quadrupole. There is a local maximum above the trap axis at $y = y_m = \frac{\sqrt{3+4\sqrt{3}}}{2}$ with $\Upsilon_s(0, y_m) = \frac{1}{7+4\sqrt{3}}$. This gives a trap depth that is lower by a factor of $3(12 + 7\sqrt{3}) \approx 72$ than that of the standard quadrupole trap.

To make an estimation more appropriate for finite-sized conductors, we consider cylindrical, perfectly-conducting electrodes that approximate equipotentials due to the line charges considered above. In the surface configuration, more charge must be placed on the inner two wires relative to the outer two wires in order to obtain equipotentials of the same diameter around all four wires. These equipotentials can be made the same size as those in the four-rod geometry, and the near circularity of the equipotentials is such that the vertical and horizontal diameters differ by only a few percent. We numerically estimate that the inner two wires must have approximately 1.35 times the charge of the outer two for an electrode diameter of 0.2 (0.2 times the distance between electrode centers). With this consideration, the above analysis can be repeated, and we obtain trap axes at the locations $(0, \pm 1.18)$ and local maxima at the locations $(0, \pm 1.96)$. The curvature at the minima leads to a secular frequency approximately 0.16 times that in a similar four-rod trap, and the trap depth is smaller by a factor of approximately 200.

Appendix B: Limits to miniaturization

With any miniaturizable ion trap geometry, one may ask how small the electrode structures can be made. Here we calculate a lower-length-scale limit, neglecting motional heating effects and ignoring the requirement of optical access for laser cooling. We assume stable trapping,

and thus fix the normalized trap strength parameter q_i (Eq. 4). For a particular ion species, this leads to constraints on the applied RF potential amplitude and frequency as R gets smaller (here we take R to be the approximate trap size). These constraints in turn restrict the trap depth U_{\max} , which must shrink as the trap size is reduced. The following discussion concerns traps of the standard quadrupole geometry (Fig. 2) for singly-ionized species. Parameters for the other trap structures mentioned above can be derived from the results of Sec. 5.

If we demand that q_i remain fixed as R is reduced, then from Eq. 4,

$$\frac{V_0}{\Omega^2} = \frac{mq_i}{2Q}R^2. \quad (\text{B.1})$$

The potential amplitude must be made to scale as $V_0 \propto R$ to ensure that the electric field amplitude at the surfaces of the electrodes $E_0 = V_0/R$ will not grow, leading to breakdown, as the trap electrodes get smaller (here we have assumed spherical electrode surfaces of radius R , relevant for the truncation of electrodes or for junctions in an array). From this follows the condition that the RF frequency must scale as $\Omega \propto R^{-1/2}$.

The trap depth is equal to the value of the pseudopotential at the location of the lowest nearby maximum; this location is displaced from the trap minimum by approximately R in all geometries studied, and will be proportional to R in any case. Thus, from Eq. 2, the trap depth is

$$U_{\max} = \frac{\beta Q^2 V_0^2}{4m\Omega^2 R^2}. \quad (\text{B.2})$$

Here β is a geometrical factor dependent on exact electrode shape. From Eqs. B.1 and B.2, we get

$$U_{\max} = \frac{\beta q_i Q}{8} V_0 = \frac{\beta q_i Q}{8} E_0 R. \quad (\text{B.3})$$

The ion trap will cease to be useful when $U_{\max} \approx \hbar\omega_i$, that is, when there is only one trapped state in the harmonic well. The secular frequency ω_i is approximately equal to $q_i\Omega/2\sqrt{2}$, which for constant q_i is

$$\omega_i = \frac{1}{2} \sqrt{\frac{q_i Q E_0}{mR}}. \quad (\text{B.4})$$

The ratio $U_{\max}/\hbar\omega_i$ scales as $R^{3/2}$ and will be given by

$$\frac{U_{\max}}{\hbar\omega_i} = \frac{\beta}{4\hbar} \sqrt{q_i Q m E_0} R^{3/2}. \quad (\text{B.5})$$

Taking values of $E_0 = 10^6$ V/m and $q_1 = 0.21$ for a beryllium ion ($m = 9$ u) trapped in a four-rod quadrupole with $\beta = 0.34$ (as in the electrode size and configuration depicted in Fig. 2), the trap will support at least one vibrational state (at a secular frequency of approximately 2.9 GHz) for $R \gtrsim 1.7$ nm. A more realistic limit might be somewhat larger: for $U_{\max}/\hbar\omega_i = 100$, $R \approx 37$ nm, for instance. Current traps do not operate near the breakdown electric field ($E_0 \approx 10^9$ V/m [7, 50]), so smaller traps are possible with higher maximum fields E_0 . Figure B.1 shows the trap depth and secular frequency for different trap sizes and several values of E_0 up to 10^9 V/m, where field emission is possible. Operating slightly below

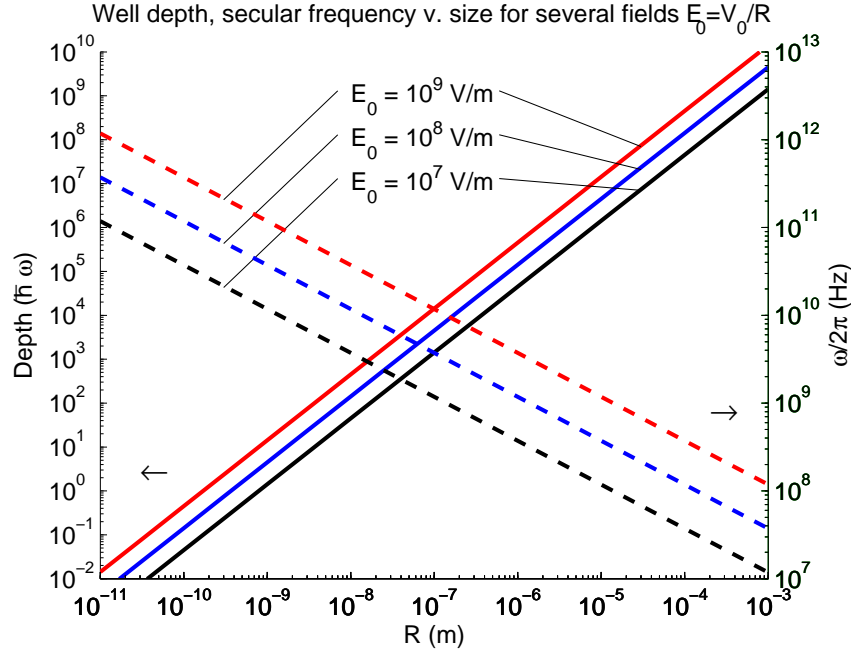


Fig. B.1. Trap depth and secular frequency as a function of trap size R for several maximum field values E_0 . The solid lines are depth, graphed on the left axis in units of $\hbar\omega$, and the dashed lines are secular frequency $\omega/2\pi$, graphed on the right axis. For this graph, $q_i = 0.21$, $m = 9$ u, and $\beta = 0.34$.

this field, trapping structures may shrink to $R \approx 0.2$ nm before there are no trapped states. At this point, the secular frequency would be a few hundred gigahertz, with a required drive frequency of approximately 13.5 times larger. Traps with weaker intrinsic trapping potentials compared to the four-rod quadrupole (such as all the other designs suggested here) will have suitably larger minimum sizes using the criteria presented here.

A recent proposal for scaling ion traps to the submicrometer scale suggests using nanomechanical resonators (possibly even carbon nanotubes) as trap electrodes and trapping an ion at a distance of $R = 100$ nm from these electrodes [51]. The authors do not consider trap depth in this work, and we point out that such a trap would most likely need to be loaded from a larger structure, as the depth may not be sufficient for initial ion capture.

Appendix C: Substrate/insulator material properties

Table C.1 lists values of pertinent properties for a selection of materials both currently used and suggested for use as insulators or substrates in the construction of microfabricated ion traps. These values are approximate and are only intended to give an idea of the relative merit of particular materials.

Table C.1. Substrate material properties. Values are given for readily available substrates at approximately room temperature for frequencies in the RF range. In general, properties of the crystalline materials vary in different directions or with different substrate orientations; values are approximate. Properties of semiconductors will vary greatly as a function of doping; values are for low or intrinsic levels of doping. These values were obtained from various published and unpublished sources.

Material	Thermal conductivity (W/(m K))	Electric resistivity (Ω cm)	Dielectric constant	Dissipation factor ($\tan \delta$)	Surface roughness (nm)	Dielectric strength (kV/mm)
AlN	180	1×10^{13}	8.5	3×10^{-4}	50	16
Alumina (99.5 %)	30	1×10^{14}	9.8	1×10^{-4}	50	20
BN	28	1×10^{13}	4.1	5×10^{-4}	50	30
Diamond	2000	1×10^{14}	5.7	6×10^{-4}	50	1000
Fused silica	1	1×10^{16}	3.9	4×10^{-4}	2	40
GaAs	55	1×10^8	13	1×10^{-3}	25	40
Quartz	7	1×10^{16}	4.5	2×10^{-4}	2	80
Sapphire	45	1×10^{14}	11	1×10^{-4}	10	35
Si	150	1×10^5	12	5×10^{-3}	25	30
SiC	250	3×10^5	14	2×10^{-1}	50	300